Non-linear force-free field modeling of a solar active region around the time of a major flare and coronal mass ejection

C.J. Schrijver[1], M.L. DeRosa[1], T. Metcalf[2], G. Barnes[2], B. Lites[3], T. Tarbell[1], J. McTiernan[4], G. Valori[5], T. Wiegelmann[6], M.S. Wheatland[7], T. Amari[8], G. Aulanier[9], P. Démoulin[9], M. Fuhrmann[10], K. Kusano[11], S. Régnier[12], J.K. Thalmann[6]

ABSTRACT

Solar flares and coronal mass ejections are associated with rapid changes in field connectivity and powered by the partial dissipation of electrical currents in the solar atmosphere. A critical unanswered question is whether the currents involved are induced by the motion of pre-existing atmospheric magnetic flux subject to surface plasma flows, or whether these currents are associated with the emergence of flux from within the solar convective zone. We address this problem by applying state-of-the-art nonlinear force-free field (NLFFF) modeling to the highest resolution and quality vector-magnetographic data observed by the recently launched Hinode satellite on NOAA Active Region 10930 around the time of a powerful X3.4 flare. We compute 14 NLFFF models with 4 different codes and a variety of boundary conditions. We find that the model fields differ markedly in geometry, energy content, and force-freeness. We discuss the relative merits of these models in a general critique of present abilities to model

[1] Lockheed Martin Advanced Technology Center, Palo Alto, Ca., USA;

[2] Colorado Research Associates, Boulder, Co., USA;

[3] High Altitude Observatory, National Center for Atmospheric Research, Boulder, Co., USA;

[4] Space Sciences Laboratory, University of California, Berkeley, USA;

[5] Astrophysikalisches Institut Potsdam, Potsdam, Germany;

[6] Max-Planck Institut für Sonnensystemforschung, Katlenburg-Lindau Germany;

[7] School of Physics, University of Sydney, Australia;

[8] CNRS, Centre de Physique Theorique, Ecole Polytechnique, Palaiseau, France;

[9] LESIA, Observatoire de Paris, CNRS, UPMC, Université Paris Diderot, Meudon, France;

[10] Universität Potsdam, Institut für Physik, Potsdam, Germany;

[11] Earth Simulator Center, Japan Agency for Marine-Earth Science and Technology, Yokohama, Japan;

[12] School of Mathematics and Statistics, University of St. Andrews, Fife, UK.

the coronal magnetic field based on surface vector field measurements. For our application in particular, we find a fair agreement of the best-fit model field with the observed coronal configuration, and argue (1) that strong electrical currents emerge together with magnetic flux preceding the flare, (2) that these currents are carried in an ensemble of thin strands, (3) that the global pattern of these currents and of field lines are compatible with a large-scale twisted flux rope topology, and (4) that the $\sim 10^{32}$ erg change in energy associated with the coronal electrical currents suffices to power the flare and its associated coronal mass ejection.

Subject headings: Sun: activity, Sun: magnetic fields, Sun: flares, Sun: corona

1. Introduction

Solar flares and coronal mass ejections derive their energy from electrical currents that run through the solar outer atmosphere. There is growing evidence that the strong electrical currents involved in major flaring tend to emerge embedded within magnetic flux after being generated within the solar convection zone, rather than being induced by the displacement of pre-existing magnetic flux by plasma flows on the surface (e.g. Leka *et al.* 1996; Wheatland 2000; Démoulin *et al.* 2002b; Démoulin *et al.* 2002a; Falconer *et al.* 2002; Leka and Barnes 2003a,b; Schrijver *et al.* 2005; Wiegelmann *et al.* 2005; Régnier and Canfield 2006; Jing *et al.* 2006; Schrijver 2007). The high-resolution vector-magnetographic capabilities of the recently launched Hinode satellite, and the advances in computational capabilities to model and analyze the atmospheric magnetic fields based on these surface field measurements, should enable us to make significant advances in addressing this problem.

Aside from flares and eruptive events, the magnetic field in the solar corona evolves slowly as it responds to changes in the surface field, implying that the electromagnetic Lorentz forces in this low-β environment are relatively weak and that any electrical currents that exist must be essentially parallel or anti-parallel to the magnetic field wherever the field is not negligible. The problem of determining the coronal field and its embedded electrical currents thus leads to the problem of reconstructing the 3D magnetic field from the observed boundary conditions, without having to deal with the effects of plasma forces on that field.

The vertical component of coronal electrical currents entering the corona from below the photosphere can in principle be deduced from the tangential components of the vector-magnetic field at the base of the corona. When combined with the vertical magnetic field component and the condition that there are at most small Lorentz forces (i.e., that the field is

"force free"), the resulting model for the current-carrying coronal field is commonly referred to as a nonlinear force-free (NLFF) field. Modeling such a field is in itself a difficult problem that requires that a number of steps be taken successfully, as outlined below (see also, e.g., Sakurai 1989; McClymont *et al.* 1997; Amari *et al.* 1997).

First, the measured polarization signals need to be inverted to form a vector-magnetogram, which requires detailed models of radiative transport of polarized light through the solar atmosphere.

Second, the procedure involves resolving an intrinsic 180° ambiguity in the components perpendicular to the line of sight, which result from a degeneracy of the polarization properties. As the electrical currents that penetrate the photosphere are carried by compact flux tubes or potentially by fine structures within sunspots, knowledge of the small-scale gradients in the field components tangential to the solar surface is critical. Several procedures have been developed to address this problem (see Section 2 for select references), all of which involve a subjective choice, either on how to deal with discontinuities interactively, or on what functional to use in an automated iterative procedure.

Third, the Lorentz forces at the base of the corona (caused by buoyancy forces and drag forces from surface plasma flows) must be dealt with, because formally the assumption that currents and field are collinear is valid only above the lower chromosphere (Metcalf *et al.* 1995), where the plasma β rapidly lies well below unity at least within the strong-field core of active regions. This step, often referred to as preprocessing, also involves subjective choices about how the field may be modified to remove net forces and torques while smoothing and tilting the observed vector field. A parallel study by Wiegelmann *et al.* (2007) confirms the expectation by Metcalf *et al.* (2007) based on a model test case that successful preprocessing distorts the observed photospheric field to an approximation of the chromospheric field.

Fourth, the NLFF field computation requires a numerical code to determine a coronal field that is compatible with the observed boundary condition. This, too, involves choices about the iteration scheme itself and about the application of boundary and initial conditions. All of these affect the outcome, even in the case of "perfect knowledge," as shown by the tests performed by Schrijver *et al.* (2006) and Metcalf *et al.* (2007).

In a series of precursor studies, we have addressed the above set of problems (e.g., Metcalf 1994; Wiegelmann *et al.* 2006; Schrijver *et al.* 2006; Amari *et al.* 2006; Metcalf *et al.* 2007, and references therein). We here proceed with an application of the developed methodology to state-of-the-art solar observations.

2. Observations

The Solar Optical Telescope (SOT) on board the Hinode spacecraft (Kosugi *et al.* 2007) observed AR 10930 in the chromospheric Ca II H channel and in the near-photospheric G band, while also obtaining magnetogram sequences for over a week with near-continuous coverage (see Figs. 1 and 2; the region's evolution is also described by, e.g., Zhang *et al.* 2007). These and other observations show that AR 10930 exhibited only B- and C-class flares from 2006/12/08 through 2006/12/13, when an X3.4 flare, peaking in soft X-rays at 2:40 UT, ended this relatively quiet period. At the time of the flare, the region was at 23° west and 5° south of disk center, and thus well positioned for vector-magnetographic observations.

If we look at this earliest phase in the flare, the very first brightenings in the chromosphere (in Ca II H) are visible at 02:04 UT over a pair of converging concentrations of opposite sign in the line-of-sight magnetic field (at position A in Fig. 2d). Twelve minutes later, three flare ribbons are evident over opposite line-of-sight magnetic polarity (Fig. 1b): at position E and at the penumbral edges at positions B and D in Fig. 2c). Such flare ribbons are commonly interpreted as the sites where energetic flare particles impact the lower atmosphere, thereby identifying the photospheric end points of the field lines on which these particles are accelerated during the energization of the flare. Hinode/XRT observed an early bright soft X-ray feature over the first chromospheric brightening (near E in Fig. 2c). The east-west bright X-ray ridge (below the center in Fig. 1a) straddles the emerging flux ends on the northern early flare ribbon near position B in Fig. 2c and on the southern one near position D around 02:15 UT. The overlying higher arched loops do not exhibit bright ribbons until approximately 2:30 UT (at positions C and near D in Fig. 2c); conversion of its excess energy into particle kinetic energy apparently starts only some 25 min after the first impulsive energy conversion.

In the days leading up to the X3.4 flare, the main changes in AR 10930 comprised a strong eastward motion of the smaller, southern sunspot relative to its larger neighbor to the north. Flux emergence between the two spots, as well as in the area west of that, continued strongly from the early hours of 2006/12/10 through the second half of 2006/12/14. Towards the end of that period, the southern spot was moving rapidly eastward, while multiple ridges of both polarities showed up between the northern and southern spots, some even forming interpenumbral connections. Snapshots of four Hinode magnetograms taken with the Narrow-band Filter Imager (NFI) are shown in Fig. 2. Note that the NFI signal is highly non-linear within the spot umbrae, where the very strong field causes the signal to fade back to zero; this does not happen in the spectrum-based vector-magnetographic SP data (described below) that we use as input for our NLFFF methods. We show a selection of the NFI images here, because they are part of a movie (see below) with magnetograms

taken at a cadence of two minutes, whereas there is an interval of 8 h between the SP maps before and after the flare.

Figure 2 shows only a small area around the sunspots at 4 h intervals up to the start of the X3.4 flare. These panels suggest relatively little change over time. The overall appearance, in fact, changes so little that we use the lower two panels to show the detailed positions of the early flare ribbons and the modeled electrical currents described in detail below. But the field is, in fact, very dynamic: successive generations of ridges and concentrations of flux form and disappear along the region between the spots and in the spots' adjacent penumbrae. This evolution can be seen in an 8 d movie in the electronic addenda, with 2 min between successive magnetograms (shown rebinned to a 1,000 by 500 pixel movie at 1/4 of the full instrumental resolution).[1]

The evolution of the emerging field between the spots is characterized by the frequent occurrence of opposite-polarity ridges, either next to each other, offset along their length, or separated by a strip of weaker line-of-sight field. Such nearly parallel strands are a characteristic signature of emerging flux bundles that carry currents along their core (see, e.g., Fig. 2 in Magara 2006, for simulations of an emerging flux rope). Such fibril electrical currents cause the magnetic field to spiral about the axis of a flux rope, so that when this flux rope breaches the solar surface, two ridges are observed where the spiraling field points upward and downward in two mostly parallel ridges in close proximity on either side of the rope's axis. We return to this point in the discussion of the model field.

In addition to the filtergram sequences, the SOT Spectro-Polarimeter (SP) obtained maps of the central regions of AR 10930 before and after the X3.4 flare. A pre-flare map was obtained between 20:30 UT and 21:15 UT on 2006/12/12, and a subsequent post-flare map between 3:40 UT and 4:40 UT on the next day; both have 0.3 arcsec pixels, and span 1024 steps with 512 pixels along the north-south oriented slit.

These Hinode SP data were prepared by the standard "SP_PREP" (Lites *et al.* 2007a) available through SolarSoft, and the resulting polarization spectra inverted to a vector magnetic field map using an Unno-Rachkovsky inversion with a Milne-Eddington atmosphere (Skumanich and Lites 1987; Lites and Skumanich 1990; Lites *et al.* 1993). Pixels with a net polarization below the threshold required for full inversion, but still with measureable Stokes V, are treated in the following manner: a longitudinal flux density is derived (see, for example, Lites *et al.* 2007b), and assuming that the field in these regions is in fact radially directed, the observing angle allows the azimuths and inclinations to be determined in the

[1]The movie is also available at http://www.lmsal.com/∼schryver/NLFFF/HinodeNFI_X3.4.mov. A smaller version covering a 2h h interval around the flare is also available.

observer's frame. In this manner, less than 0.5% of the pixels in the map are undetermined and discontinuities due to the thresholds are minimized.

The vector magnetic field maps are then subjected to an ambiguity resolution approach which uses simulated annealing to minimize a functional of the electric current density and divergence-free condition (Metcalf 1994). The algorithm applied includes the enhancements described in Metcalf *et al.* (2006), and was the top-performing automated method amongst those compared in that same study. The ambiguity resolution appears to work successfully for most of the field of view, and leaves only a few very small patches where the transverse field changes discontinuously. We cannot tell whether these patches are artifacts or real, and consequently do not attempt to remove them from the processed vector field. The vertical components of the SP vector-magnetic field before and after the flare are shown in Figs. 1c and 1d, respectively. Maps of the vertical current density, j_z, are shown in Figs. 1e, and f; we note that the overall currents are balanced to within 0.7% in the field of view, while the currents within each polarity reveal a net current between the field polarities of approximately 20% for positive B_z and 15% in the negative polarity. The line-of-sight components of the central area as measured by the NFI are shown enlarged in Fig. 2. We note that the polarity patterns seen in the filter-based NFI data match those in the spectrum-based SP vector magnetograms (the latter are available as addenda to the electronic edition of this paper[2]), as expected for subsonic flows affecting fields observed at 120 mÅ away from the line center position at 6302 Å.

We embedded the Hinode/SP maps in a much larger, lower-resolution SOHO/MDI (Scherrer *et al.* 1995) line-of-sight magnetogram in order to incorporate information on flux outside the SP map, subject to the current-free (potential) approximation. In order to be able to apply the NLFF codes with present computational resources, the data are rebinned 2×2, to 0.63 arcsec pixels. A Green's function potential field (Metcalf *et al.* 2007) is computed for the entire expanded area to serve as initial condition, and as side- and upper-boundary conditions (where applicable for the methods; see Metcalf *et al.* (2007)). The central area of 150 × 150 Mm (203 × 203 arcsec, or 320 × 320 pixels) is extracted for modeling, together with the corresponding potential-field cube over 256 vertical pixels.

[2]FITS files are also available at http://www.lmsal.com/∼schryver/NLFFF/; the file contents is described in the FITS header comment field.

3. NLFFF modeling

We apply the four NLFF field algorithms described in Schrijver *et al.* (2006) and, where modified, by Metcalf *et al.* (2007): the weighted optimization algorithm by Wiegelmann (2004), the uniformly weighted optimization model as implemented by McTiernan (Wheatland *et al.* 2000), the magneto-frictional code by Valori *et al.* (2005), and the current-field interaction method by Wheatland (2006, 2007, and references therein). For the Wheatland method, three solutions are computed with different boundary conditions on vertical current: currents are chosen from regions with positive vertical field B_z; from regions with negative vertical field; and based on an average of those two.

Apart from working with the observed (disambiguated) vector fields, we also apply preprocessing to the lower boundary vector field. This removes net magnetic forces and torques which should not exist in the model. The preprocessing is performed with a method devised by Metcalf *et al.* (2007), which leaves B_z unchanged, and one by Wiegelmann *et al.* (2006), which allows all field components to change. Both of these are applied with and without spatial smoothing. The characteristic value of the rms difference between observed and preprocessed values for $B_{x,y}$ are $\sim 15\%$ of the standard deviation in $B_{x,y}$. A summary of these preprocessing algorithms is included in Metcalf *et al.* (2007).

The work by Metcalf *et al.* (2007) showed that the additional step of preprocessing the observed photospheric vector-magnetic data resulted in a marked improvement in the agreement between the resulting NLFFF extrapolations and their model reference field. They argue that this result likely stems from the fact that the preprocessed photospheric field is a good approximation of the corresponding chromospheric field, where the Lorentz forces are much weaker. This is confirmed by Wiegelmann *et al.* (2007) in a detailed evaluation of the preprocessing process. As in the earlier study, we find here that the best fits are obtained for preprocessed data. We return to this topic in Section 4.

Using these algorithms, we obtain 14 distinct model fields, summarized in Table I. We use two different measures to identify the model that best fits the observed corona, and one that identifies the most internally consistent force-free field; all to these identify the same model field as "best."

A subjective goodness-of-fit is provided visually by comparing the TRACE and Hinode/XRT images with the computed field lines, and assessing the match for five characteristic signatures of the field, labeled in Fig. 1a as follows: 1) the sheared arcade between the spots, 2) the eastern arch of loops around the southern spot, 3) the low, nearly horizontal field west of the southern spot, 4) the arcade high over that horizontal field, and 5) the absence of shear around the emerging flux northwest of the northern spot. Table I shows the model fields

ordered by the resulting metric $Q_{\rm m}$: each good or poor correspondence contributes a bonus or penalty to the metric of $+1$ or -1, respectively, while an ambiguous correspondence is not weighed in the value of $Q_{\rm m}$. Only the Wheatland positive-field solution (Wh^{+}_{pp}) applied to a preprocessed lower boundary (including spatial smoothing) successfully reproduces all five of these features.[3]

A second, objective measure for the goodness of fit is based on finding field lines in the models that best match a set of identified coronal loops in the Hinode/XRT and TRACE coronal images, and computing the deviation between these in projection against the solar disk. Coronal observations of AR 10930 were made both with Hinode's XRT using its thin-Be/open filter wheel setting, and with TRACE (Handy *et al.* 1999) in its 195 Å passband, both with 1 arcsec pixels. In order to increase the signal-to-noise level, we use the geometric mean of sets of exposures, as shown in Fig. 1a, for loop tracing. These loop traces are then compared to 100 field lines computed for each of the model fields with starting points distributed within the modeled volume along the line of sight through the midpoint of each traced loop i. For each of these field lines, we compute the area contained between the corresponding loop trace and the field line projected against the plane of the sky; this area A_i is bounded by line segments that connect the ends of the traced loops to the nearest points on the projected field lines. The field lines with lowest value for A_i are selected as the best-fit field lines for each traced loop. The model field with the lowest total value $\Sigma_i \min(A_i)$ for the set of traced loops is identified as the best model. Formally, the best fitting model field is again the Wh^{+}_{pp} solution, but Fig. 1a shows that the correspondence between model field and corona is far from perfect - we return to this issue in Section 4.

A final criterion is based on the consistency of the model field with the properties of a truly force-free field: the Wh^{+}_{pp} solution also has the lowest residual Lorentz forces (as measured by a current-weighted angle between magnetic field and electrical current), while being among the solutions with the lowest average absolute divergence of the model field (both of these metrics should equal zero for a perfect field). Table I lists the values of these metrics. Note that the metrics for field divergence are naturally grouped by NLFFF algorithm type.

In the present study, the Wheatland Wh^{+}_{pp} model outperforms that of the weighted-optimization algorithm by Wiegelmann that provided the best solutions in our earlier two trial studies (Schrijver *et al.* 2006; Metcalf *et al.* 2007). Based on this single application,

[3]Renderings of seven of the NLFFF models and of the potential-field extrapolation for the pre-processed pre-flare fields are shown in the electronic addenda. These images are also available at http://www.lmsal.com/∼schryver/NLFFF/.

we cannot identify why the Wh_{pp}^{+} model performs best. In fact, we note that the current-field iteration procedure does not converge to a fixed field for any of the various boundary conditions, but rather oscillates. The code was run for 20 iterations in each case, at which stage the field is still changing at successive iterations (on average by 2% in the vector norm), although the energy was found to vary only slowly over the final iterations. We note that this was also seen for an analysis of test fields for a similar Grad-Rubin-based method by Amari *et al.* (2006). Despite this, the Wh_{pp}^{+} model is still the best model field. We expect that it performs best among the other Wheatland solutions owing to the following property: The Wheatland code requires that no electrical currents leave the volume. As the lower-boundary vector field over-determines the solution, the code uses the boundary current information either where B_z is positive or where it is negative, and then only where the field strength exceeds 5% of the maximum value and where the horizontal field changes its azimuth by less than 120° between neighboring pixels (this criterion is intended to limit the spurious currents associated with incorrect disambiguations of the perpendicular field component). The field lines with $B_z > 0$ primarily emanate from the smaller, southern spot, which mostly close within the volume without major problems. This allows the Wh_{pp}^{+} solution to achieve a highest-fidelity representation of the real coronal field, in marked contrast to the $Wh_{\rm pp}^{-}$ solution for $B_z < 0$, in which the field is highly distorted.

In a comparison with other methods, we note that the Wiegelmann and McTiernan algorithms attempt to find a solution by minimizing a functional that includes a non-zero divergence of the magnetic field (and thus indirectly a source for electrical currents). Thus, magnetic flux and electrical currents can originate within the model's volume, in particular near the lower boundary where many of the currents of interest run. Similarly, the Valori code can allow for higher values in the field's divergence in the attempt of attain lower residual Lorentz forces. The Wheatland code makes use of a vector potential, and thus has an intrinsically low divergence (compare the values in columns 5 and 8 in Table I, see also Wheatland (2007)). Whereas this yields a model field that best meets the formal requirement of being force free, one might have expected that the artificial sources would provide other methods additional freedom to find a better matching field. But it apparently does not.

We defer further discussion of the relative performance of the various methods to a later study, in which the effects of different base vector-magnetic fields and instrumental fields of view need to be compared for a much larger sample of observations which, at present, does not yet exist. We can add one observation on the potential effect of the field of view. The $Wh_{\rm pp}^{+}$ algorithm was also applied to a vector-field footprint extended westward to include the relatively small amount of flux in the leading part of the region that appears to be involved in the post-eruption arcade. This extension makes the footprint twice as wide, and required lowering the model volume by a factor of two to maintain the demand on computer memory.

The $Wh^{+}_{\rm pp}$ pre-flare model field for this extended footprint is very similar to the model field discussed above, both in terms of field lines and in terms of electrical currents, although the free energy is lower by some 5%. We conclude that our inferences discussed below about the pre-flare field configuration are not affected significantly by our choice of the field of view. The $Wh^{+}_{\rm pp}$ model for the extended post-flare configuration did not converge; that aspect will require substantial further study.

4. Discussion and conclusions

The best-fit Wh^{+}_{pp} model NLFF field suggests that, prior to the flare, the strongest electrical currents run between the main spot groups. These currents connect the penumbrae through filamentary currents that arch up to $h \approx 12\,$Mm over low-lying current strands that lie within $h \approx 6\,$Mm over the emerging field between the spots. Not surprisingly, the bulk of the free energy (i.e., the energy in excess of that of the minimum-energy state given by the purely potential field) is associated with these electrical currents (Figs. 1c, d, and 2). The main current strands connect footpoints that are well separated, and that traverse a substantial distance over and along the region of emerging flux between the spots. They connect the emerged and emerging flux adjacent to the southern spot to the umbra of the northern spot (Fig. 2c, and the top panels in Fig. 3).

In the best-fit Wh^{+}_{pp} model, a low-lying, compact structure of current-carrying emerging flux lies below the main current arcade in the region containing opposite-polarity ridges of vertical field (see the perspective volume renderings in Fig. 3a, and also Fig. 4c). This is the site at which the energy release in the X3.4 flare starts its impulsive phase (see Fig. 2c, d).

The flare appears to tap energy from most of the flux system that has emerged over the preceding days: the currents in the relatively high arching arcade are drastically weakened after the flare (Fig. 4a, b), whereas the long fibril of concentrated current low above the solar surface completely disappears (Fig. 4c, e). We interpret the flare/CME as a cataclysmic energy drain from a current-carrying flux rope that emerged from below the photosphere. The complex field evolution with many mixed-polarity ridges that is observed in the Hinode/NFI magnetogram sequence suggests that the flux rope is either a bundle of smaller strands wrapped about each other, or a single rope with internal structure both in terms of field strength and current density. The 8 h interval between the SOT-SP vector magnetograms is far too long to address this issue.

With the Wh^{+}_{pp} NLFFF model in hand, what can we say about the topology of the pre-eruptive magnetic field? The field line plots in Fig. 3 can be interpreted as a low altitude

sheared arcade between the spots underneath an essentially potential field that is nearly orthogonal to the arcade; such a configuration has been described by, e.g., DeVore and Antiochos (2000). When considering the counterclockwise rotation of the southern, positive-polarity sunspot evident in the NFI movie (see the electronic addenda) one may alternatively infer an overall twisting of the magnetic field, as has been observed, for example, by TRACE for the corona over some rotating sunspots (see, e.g., Brown *et al.* 2002). Several distinct conceptual models exist for such flux ropes. One of these is for "included" flux ropes which have strong internal axial fields (that carry at most weak currents) separated from an external field by a current layer (this concept was used in the study by Metcalf *et al.* (2007). Another is for "circuit" flux ropes that are produced by (thick or thin) net currents along their axes surrounded by field lines that spiral about the current (e.g., Titov and Démoulin 1999; Török and Kliem 2007). Then there are "twisted" flux ropes, that either may emerge as such (e.g., Fan and Gibson 2004; Amari *et al.* 2004) or may form from photospheric vortical motions (e.g., Amari *et al.* 1996; Török and Kliem 2003; Aulanier *et al.* 2005). These should show a large-scale bipolar direct current pattern surrounded by external return currents (i.e., currents with opposite direction within the same magnetic polarity); the existence of such patterns continues to be debated (see Wheatland 2000, and references therein).

A potential discriminator for the applicability of any of these concepts to AR 10930 is the distribution of pre-eruptive photospheric and coronal electric currents as deduced from the vector magnetograms (Fig. 1e) and the NLFF field model (Fig. 4a, c, and e). On the scale of the entire active region, the current pattern in AR10930 bears a striking resemblance to that of "twisted" flux ropes. Comparing the pre-flare column of Fig. 4 with those of Figs. 9 and 10 in Aulanier *et al.* (2005), we see (1) a swirling bipolar pattern in j_z in and immediately above the photosphere, with concentrations at the sunspots, and arching around the spots to form parallel lanes of vertical current located on both sides of the large-scale neutral line between the spots; (2) narrower and fainter return currents away from the main neutral line on the edges of the current concentrations; (3) an elongated strong patch in the coronal currents right at the neutral line with essentially horizontal currents and field. In contrast, the current pattern of AR 10930 does not match that expected for the other types of flux ropes: sheared arcades are associated with parallel lanes of direct and return currents, "included" ropes mostly show a single current shell whose photospheric footpoints result in narrow parallel lanes, and "circuit" flux ropes show unidirectional currents only.

In this picture, the pre-eruptive compact current carrying structure, at the location of the strong soft X-ray emission observed before and during the flare, would simply trace the shortest twisted field lines of a large-scale twisted flux rope. This is based on the expectation that a given end-to-end twist applied to short, low field lines results in stronger currents than when the same twist is applied to longer, higher field lines (Aulanier *et al.* 2005).

The interesting similarity of our model field to theoretical models of twisted flux ropes, while consistent with the evolution seen in the NFI magnetograms, is encouraging, but will require confirmation beyond this single example. The relative roles of pre-existing twist below the photosphere and any added twist during the emergence associated with plasma flows will need to be assessed. Moreover, the current pattern shown in Fig. fig:4 clearly shows a strong degree of filamentation, which might have non-negligible consequences in terms of field topology. This filamentation may be a consequence of a process that is conducive to generating smaller scales (including, e.g., the convective collapse upon emergence), or may in fact hold the key to another formation process for the overall configuration.

The best-fit Wh^{+}_{pp} solutions for the pre- and post-flare observations show a decrease in the free energy from 32% of the potential-field energy to a post-flare configuration with only 14% in excess of the potential field model for the post-flare state (Table I). This corresponds to a drop in free energy of 3×10^{32} ergs, even as the total field energy in the potential field extrapolation shows an increase by $\sim 10^{32}$ ergs due to the continuing emergence of flux in the 8 h interval between the SOT-SP maps. This decrease in free energy is adequate to power an X-class flare (with energies of 10^{31-32} ergs; Hudson (1991); Bleybel *et al.* (2002)) associated with a coronal mass ejection (with energies up to about 10^{32} ergs; Hundhausen 1997).

We note that the continuing emergence of flux between the pre- and post-flare SP maps not only causes the energy in the post-flare potential field to be larger than the pre-flare potential field (see last line in Table I), but also causes most model fields to have energy ratios $E/E_{\rm p,pre}$ that increase from before to after the flare. Only the best-fit Wh^{+}_{pp} model shows a drop in energy, likely because its strong pre-flare currents lose more energy than the flux emergence adds in this particular model field. Note that some model fields have energies below that of the potential field; causes for this anomaly were discussed for a test field by Metcalf *et al.* (2007).

This exercise illustrates several problematic issues with the NLFFF extrapolation process. First, the "preprocessing" of the observed vector field yields a marked improvement in the quality of most of the NLFF field models. The preprocessing is one way of reducing the effect of the Lorentz forces acting in the photosphere; further studies of how best to deal with these forces should be undertaken (along the lines of that for a model field by Wiegelmann *et al.* 2007). Second, although provided with the same boundary conditions, only one among seven model fields based on preprocessed boundary conditions matches the observed coronal field acceptably by visual inspection based on a limited set of key features (as measured by $Q_{\rm m}$ in Table I). This reveals the sensitivity to details in model implementation and boundary and initial conditions also seen in our two earlier studies (Schrijver *et al.* 2006; Metcalf *et al.* 2007). An integral part of the latter problem is, of course, the resolution

of the 180° ambiguity intrinsic to the measurement of the field component perpendicular to the line of sight (see the tests of various methods based on known model fields described by Metcalf *et al.* 2006; Li *et al.* 2007). It is clear that a systematic study of these differences between the algorithms ranging from the observations to the final NLFF field models, and their relative merits and problems, is needed to identify one or a few of the most successful strategies.

And, finally, we note that even the best-fit Wh_{pp}^{+} model provides a rather poor match to the observed coronal loops. This may be a consequence of the global nature of such loops: even if the field locally would be modeled to within a few degrees, the integration along the path of a field line could still lead to a markedly different path relative to those in the true field and to observed coronal loops. On the other hand, we note that the poor match may be a consequence of an intrinsic problem of tracing field lines by using coronal brightenings: Aulanier *et al.* (2005), for example, argue that coronal S-shaped structures associated with twisted flux ropes may not trace individual field lines, but rather are formed by an ensemble of partially outlined loops subject to line-of-sight integration.

Although we can measure the divergence of the field line relative to the observed loops, there is unfortunately no known method that quantifies how significant such path differences are in terms of the field's total energy or helicity. Both of the latter quantities are of interest to, say, space weather forecasters, but we have yet to learn how the comparison of observed loops to model field lines can be used to improve estimates of energy and helicity.

On the positive side, (1) the best-fit Wh_{pp}^{+} model field compares relatively well with the observed corona, and (2) the energy estimates and the pre-to-post flare energy difference suffices to power the flare. Consequently, we think that the best available vector-magnetographic data and NLFFF modeling techniques support our main finding:

We conclude that the filamentary electrical currents that emerge with the magnetic flux between the main sunspots in AR 10930 over a period of up to several days (1) carry enough energy to power the observed major X3.4 flare and associated coronal mass ejection, (2) are involved in earliest impulsive phase of the flare, and (3) show a substantial decrease in magnitude even as their associated field lines connect over shorter distances when comparing pre- and post-flare states. Thus, our application of nonlinear force-free field modeling to state-of-the art vector-field data on a complex active region provides strong evidence in support of the growing notion that major solar flares are directly associated with the energy carried by electrical currents that emerge from below the solar surface, and is suggestive, at least in this case, of an emerging twisted flux rope.

Tom Metcalf died in a skiing accident before this manuscript was completed; we dedicate

it to the memory of his friendship and collegiality. Hinode is a Japanese mission developed and launched by ISAS/JAXA, collaborating with NOAJ as domestic partner, NASA (USA) and STFC (UK) as international partners. CJS, MLD, TRM, and GB were supported by by Lockheed Martin Independent Research Funds. The work of TW was supported by DLR grant 50 OC 0501 and that of JKT by DFG grant WI 3211/1-1. GV was supported by DFG grant HO1424/9-1. GA and PD gratefully acknowledge financial support by the European Commission through the SOLAIRE Network (MTRN-CT-2006-035484). MSW acknowledges generous support provided by the Observatoire de Paris enabling travel to the workshop. The team thanks the CIAS of Observatoire de Paris for hosting the NLFFF4 workshop.

REFERENCES

Amari, T., Aly, J. J., Luciani, J. F., Boulmezaoud, T. Z., & Mikić, Z.: 1997, Sol. Phys. 174, 129

Amari, T., Boulmezaoud, T. Z., & Aly, J. J.: 2006, A&A 446, 691

Amari, T., Luciani, J. F., & Aly, J. J.: 2004, ApJL 615, 165

Amari, T., Luciani, J. F., Aly, J. J., & Tagger, M.: 1996, ApJL 466, 39

Aulanier, G., Démoulin, P., & Grappin, R.: 2005, A&A 430, 1067

Bleybel, A., Amari, T., van Driel-Gesztelyi, L., & Leka, K. D.: 2002, A&A 395, 685

Brown, D. S., Nightingale, R. W., Alexander, D., Schrijver, C. J., Metcalf, T. R., Shine, R. A., Title, A. M., & Wolfson, C. J.: 2002, in G. Tsiropoula, U. Schühle, and H. Sawaya-Lacoste (Eds.), *Proceedings of the workshop on Magnetic Coupling of the Solar Atmosphere (Santorini)*, ESA SP-505, ESA Publications Division, Noordwijk, The Netherlands, p. 261

Démoulin, P., Mandrini, C. H., Van Driel-Gesztelyi, L., Lopez Fuentes, M. C., & Aulanier, G.: 2002a, Sol. Phys. 207, 87

Démoulin, P., Mandrini, C. H., Van Driel-Gesztelyi, L., Thompson, B. J., Plunkett, S., Kovári, Z., Aulanier, G., & Young, A.: 2002b, A&A 382, 650

DeVore, C. R. & Antiochos, S. K.: 2000, ApJ 539, 954

Falconer, D. A., Moore, R. L., & Gary, G. A.: 2002, ApJ 569, 1016

Fan, Y. & Gibson, S. E.: 2004, ApJ 609, 1123

Handy, B. N., Acton, L. W., Kankelborg, C. C., Wolfson, C. J., Akin, D. J., Bruner, M. E., Carvalho, R., Catura, R. C., Chevalier, R., Duncan, D. W., Edwards, C. G., Feinstein, C. N., Freeland, S. L., Friedlander, F. M., Hoffman, C. H., Hurlburt, N. E., Jurcevich, B. K., Katz, N. L., Kelly, G. A., Lemen, J. R., Levay, M., Lindgren, R. W., Mathur, D. P., Meyer, S. B., Morrison, S. J., Morrison, M. D., Nightingale, R. W., Pope, T. P., Rehse, R. A., Schrijver, C. J., Shine, R. A., Shing, L., Strong, K. T., Tarbell, T. D., Title, A. M., Torgerson, D. D., Golub, L., Bookbinder, J. A., Caldwell, D., Cheimets, P. N., Davis, W. N., Deluca, E. E., McMullen, R. A., Amato, D., Fisher, R., Maldonado, H., & Parkinson, C.: 1999, Sol. Phys. 187, 229

Hudson, H. S.: 1991, Sol. Phys. 133, 357

Hundhausen, A. J.: 1997, in J. R. Jokipii, C. P. Sonnett, and M. S. Giampapa (Eds.), *Cosmic winds and the heliosphere*, University of Arizona Press, Tucson, Arizona, p. 259

Jing, J., Song, H., Abramenko, V., Tan, C., & Wang, H.: 2006, ApJ 644, 1273

Kosugi, T., Matsuzaki, K., Sakao, T., Shimizu, T., Sone, Y., Tachikawa, S., Hashimoto, T., Minesugi, K., Ohnishi, A., Yamada, T., Tsuneta, S., Hara, H., Ichimoto, K., Suematsu, Y., Shimojo, M., Watanabe, T., Shimada, S., Davis, J. M., Hill, L. D., Owens, J. K., Title, A. M., Culhane, J. L., Harra, L. K., Doschek, G. A., & Golub, L.: 2007, sp 243, 1

Leka, K. D. & Barnes, G.: 2003a, ApJ 595, 1277

Leka, K. D. & Barnes, G.: 2003b, ApJ 595, 1296

Leka, K. D., Canfield, R. C., McClymont, A. N., & van Driel-Gesztelyi, L.: 1996, ApJ 462, 547

Li, J., Amari, T., & Fan, Y.: 2007, ApJ 654, 675

Lites, B. W., Elmore, D. F., Seagraves, P., & Skumanich, A. P.: 1993, ApJ 418, 928

Lites, B. W., Ichimoto, K., Katsukawa, Y., Kubo, M., Shine, R. A., Tarbell, T. D., Kamio, S., & Shimojo, M.: 2007a, in preparation

Lites, B. W. & Skumanich, A.: 1990, ApJ 348, 747

Lites, B. W., Socas-Navarro, H., Berger, T., Frank, Z., Shine, R. A., Tarbell, T. D., Title, A. M., Ichimoto, K., Katsukawa, Y., & Tsuneta, S.: 2007b, ApJ, in press

Magara, T.: 2006, ApJ 653, 1499

McClymont, A. N., Jiao, L., & Mikić, Z.: 1997, Sol. Phys. 174, 191

Metcalf, T. R.: 1994, Sol. Phys. 155, 235

Metcalf, T. R., DeRosa, M. L., Schrijver, C. J., Barnes, G., Van Ballegooijen, A. A., Wiegelmann, T., Wheatland, M. S., , Valori, G., & McTiernan, J.: 2007, Sol. Phys., submitted

Metcalf, T. R., Jiao, L., McClymont, A. N., Alexander, N., Canfield, R. C., & Uitenbroek, H.: 1995, ApJ 439, 474

Metcalf, T. R., Leka, K. D., Barnes, G., Lites, B. W., Georgoulis, M. K., Pevtsov, A. A., Balasubramaniam, K. S., Gary, G. A., Jing, J., Li, J., Liu, Y., Wang, H. N., Abramenko, V., Yurchyshyn, V., & Moon, Y.-J.: 2006, Sol. Phys. 237, 267

Régnier, S. & Canfield, R. C.: 2006, A&A 451, 319

Sakurai, T.: 1989, Sol. Phys. 121, 347

Scherrer, P. H., Bogart, R. S., Bush, R. I., Hoeksema, J. T., Kosovichev, A. G., Schou, J., Rosenberg, W., Springer, L., Tarbell, T. D., Title, A., Wolfson, C. J., Zayer, I., & The MDI Engineering Team: 1995, Sol. Phys. 162, 129

Schrijver, C. J.: 2007, ApJL 655, 117

Schrijver, C. J., De Rosa, M. L., Title, A.M., & Metcalf, T. R.: 2005, ApJ 628, 501

Schrijver, C. J., DeRosa, M. L., Metcalf, T. R., Liu, Y., McTiernan, J., Régnier, S, Valori, G., Wheatland, M. S., & Wiegelmann, T.: 2006, Sol. Phys. 235, 161

Skumanich, A. & Lites, B. W.: 1987, ApJ 322, 483

Titov, V. S. & Démoulin, P.: 1999, A&A 351, 707

Török, T. & Kliem, B.: 2003, A&A 406, 1043

Török, T. & Kliem, B.: 2007, Astronomische Nachrichten 328, 743

Valori, G., Kliem, B., & Keppens, R.: 2005, A&A 433, 335

Wheatland, M. S.: 2000, ApJ 532, 616

Wheatland, M. S.: 2006, Sol. Phys. 238, 29

Wheatland, M. S.: 2007, Sol. Phys., in press

Wheatland, M. S., Sturrock, P. A., & Roumeliotis, G.: 2000, ApJ 540, 1150

Wiegelmann, T.: 2004, Sol. Phys. 219, 87

Wiegelmann, T., Inhester, B., & Sakurai, T.: 2006, Sol. Phys. 233, 215

Wiegelmann, T., Lagg, A., Solanki, S. K., Inhester, B., & Woch, J.: 2005, A&A 433, 701

Wiegelmann, T., Thalmann, J. K., Schrijver, C. J., DeRosa, M. L., & Metcalf, T. R.: 2007, Sol. Phys., submitted

Zhang, J., Li, L., & Song, Q.: 2007, ApJL 662, 35

Table 1: Metrics for the field extrapolations, in order of quality Q based on the visual correspondence to the coronal pre-flare image.

		pre-flare: 2006/12/12			post-flare: 2006/12/13		
Model[1]	$Q_{\rm m}$ [2]	$E/E_{\rm p,pre}$ [3]	CW sin [4]	$\langle\lvert f_i\rvert\rangle \times 10^8$ [5]	$E/E_{\rm p,pre}$	CW sin	$\langle\lvert f_i\rvert\rangle \times 10^8$
1: Wh^{+}_{pp}	5	1.32	0.24	3.6	1.19	0.18	2.0
2: Wh^{+}_{np}	3	1.10	0.27	3.9	1.23	0.27	4.6
3: Wie_{wp}	3	1.09	0.35	19.	1.18	0.32	13.
4: Val_{pp}	3	1.10	0.28	230.	1.27	0.31	190.
5: Wh^{0}_{pp}	2	1.04	0.28	3.0	1.53	0.27	3.7
6: Wie_{ns}	2	1.04	0.43	22.	1.13	0.39	30.
7: Val_{np}	2	0.88	0.29	220.	0.99	0.34	210.
8: Wie_{np}	1	0.95	0.43	24.	1.04	0.39	27.
9: Wie_{pp}	0	1.05	0.44	18.	1.15	0.39	21.
10: McT_{pp}	0	1.01	0.61	29.	1.07	0.59	25.
11: Wh^{0}_{np}	-1	1.03	0.27	2.5	1.12	0.23	2.6
12: Wh^{-}_{np}	-1	1.04	0.25	2.9	1.11	0.24	2.9
13: Wh^{-}_{pp}	-1	1.05	0.27	3.2	1.16	0.19	2.2
14: McT_{np}	-2	0.95	0.64	26.	1.00	0.61	24.
15: pot'l	-3	1	-	0.8	1.04	-	0.8

[1]Models: Wh: Wheatland, Wie: Wiegelmann, Val: Valori, McT: McTiernan; $+, -, 0$: based on positive or negative B_z, or both, respectively; np: no preprocessing; ns: preprocessed without smoothing, pp: preprocessing including smoothing; wp: Wiegelmann's preprocessing and smoothing.

[2]Quality of fit by visual inspection for five features: a good/poor correspondence for each feature adds $+1, -1$, respectively, to the total value; an ambiguous correspondence adds 0.

[3]Energy, relative to the energy in the pre-flare potential field model.

[4]Current-weighted value of $\sin\theta$, where θ is the angle between the electrical current and the magnetic field in the model solution.

[5]The unsigned mean over all pixels i in the comparison volume of the absolute fractional flux change $|f_i| = |(\nabla \cdot \mathbf{B})_i|/(6|\mathbf{B}|_i/\Delta x)$, where Δx is the grid spacing (compare Wheatland *et al.* 2000).

Fig. 1.— The chromosphere, corona, and magnetic field of NOAA AR 10930. Panel *a* shows the 320×320 pixel footprint of the full model volume for the NLFFF codes (itself surrounded by a much larger skirt of a line-of-sight magnetic map). The largest square is the 224×224 pixel area (with sides of 101 Mm) used for the energy estimates, and shown in panels *b–d* and in Figs. 3 and 4. The smaller square shows the footprint shown in Fig. 2. Panels: *a)* time-averaged Hinode/XRT soft X-ray image. Individual loops traced on this image or on a TRACE 195 Å image (not shown here) are represented in green; the best-matching model field lines for the $Wh^{+}_{\rm pp}$ model field are shown in purple. Numbers identify the characteristic signatures in the field that were used in the subjective assessment of the goodness-of-fit, as discussed in Section 3. *b)* Chromospheric Ca II H image for the onset phase of the flare. *c)* Pre-flare Hinode/SOT-SP B_z on 2006/12/12 around 21 UT. Contours show the vertically integrated energy density in the $Wh^{+}_{\rm pp}$ field minus that of the potential field; the white contour lies near the maximum value and the green contour at half that. *d)* Post-flare Hinode/SOT-SP B_z on 2006/12/13 around 4 UT. Contours as in panel *b*. *e, f)* Maps of the vertical current density j_z corresponding to the pre- and post-flare maps shown in panels *c* and *d*, respectively. The color scale for the lower four panels runs from blue (negative) to red (positive), saturating into black or white, respectively.

Fig. 2.— Time series of magnetograms showing the evolution of the line-of-sight magnetic field as observed by the HINODE Solar Optical Telescope with the Narrow-Band Filter Imager (NFI) at 4 h intervals prior to the X3.4 flare. Coordinates (with north up and - by solar-physics convention - west towards the right) are in pixels of 0.16 arcsec each; the area shown covers the central 10% of the footprint of the NLFF field model volume (compare the smallest square in Fig. 1a to its full field of view). Note that the NFI magnetograph signal is non-monotonic, disappearing in the umbrae of the two spots. Panel *d* shows in red the brightest segments of the flare ribbons seen in the Ca II H channel at 02:16:39 UT (cf., Fig. 1d); it also outlines the brightest quiescent kernel in soft X-rays seen by the Hinode X-ray telescope at the same time (green contour) and the brightest coronal structure (black contour; cf., Fig. 1a). The latter two are repeated in panel *c*, taken close to the time of the pre-flare vector-magnetogram obtained by the spectro-polarimeter. The magnetic information in that panel has been replaced by the line-of-sight integral of the vector norm of the electrical currents (cf., Fig. 4a) within the blue contour, which is where these currents are strongest.

Fig. 3.— Visualizations of the magnetic field over NOAA Active Region 10930 before (top) and after (bottom) the X3.4 flare, shown against the corresponding map of B_z. Sample field lines outline the field; white field lines close within the NLFF model volume, while colored field lines (purple or green for the two polarities of B_z at their base) leave that volume to connect to more distant regions. The rendered volumes (red) show where the electrical current densities are highest, using the same threshold level in both panels (cf., Fig. 2c).

The compact, low current system below the large, high-arching currents in the top panel corresponds to the site (position A in Fig. 2d) of the initial brightenings of the X3.4 flare and associated coronal mass ejection.

Fig. 4.— *a, b)* Vertically integrated electrical currents in the $Wh^{+}_{\rm pp}$ pre-flare (left) and post-flare (right) model fields, on the same color scale. *c, d)* As panels *a, b*, but showing the horizontal currents integrated over the lowest 6,100 km (12 pixels), using the same grey scale. *e, f)* As panels *c, d* for j_z, with white/black for positive/negative j_z, respectively.

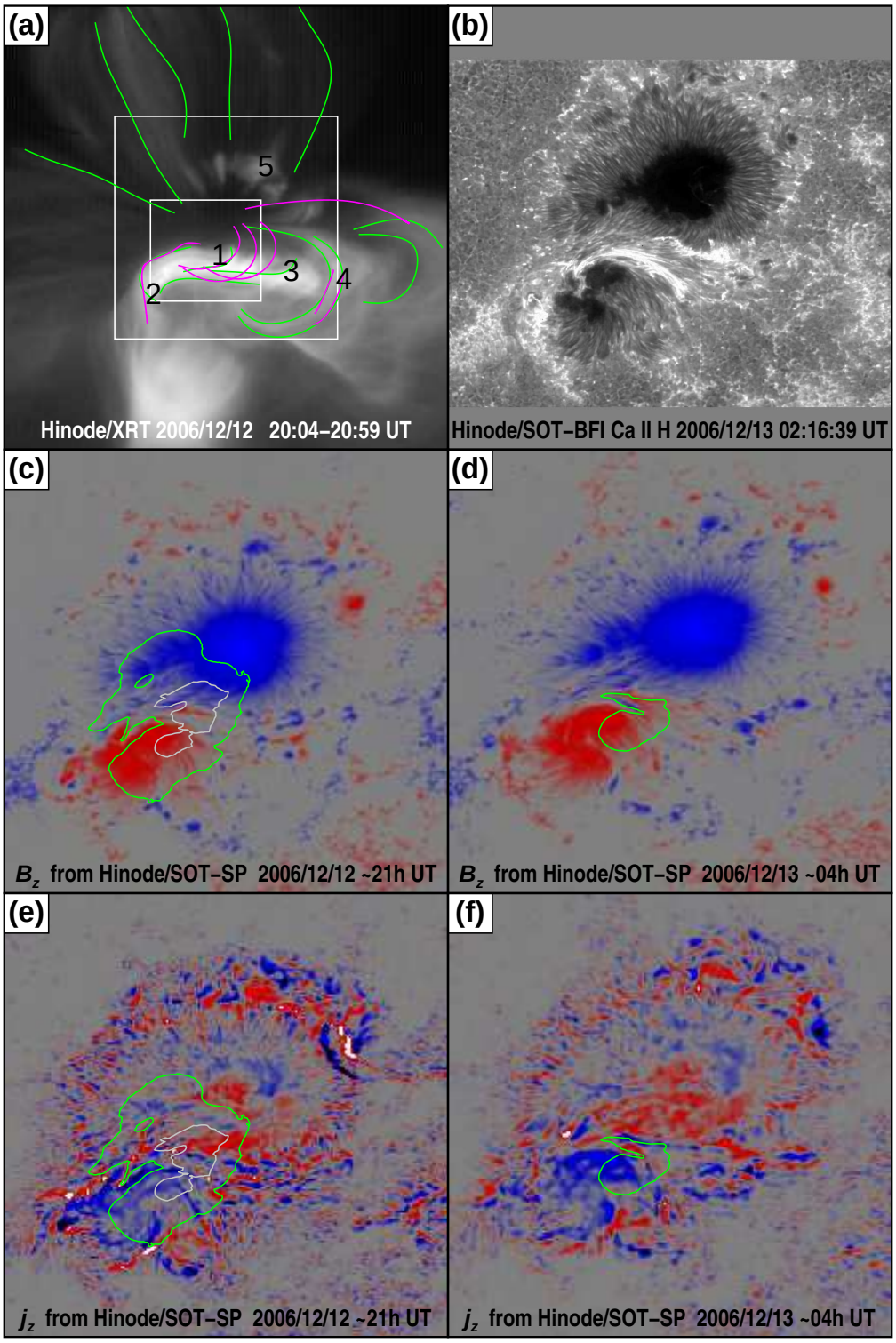
(a)
5
1
2
3
4
Hinode/XRT 2006/12/12 20:04–20:59 UT
(b)
Hinode/SOT–BFI Ca II H 2006/12/13 02:16:39 UT
(c)
B_z from Hinode/SOT–SP 2006/12/12 ~21h UT
(d)
B_z from Hinode/SOT–SP 2006/12/13 ~04h UT
(e)
j_z from Hinode/SOT–SP 2006/12/12 ~21h UT
(f)
j_z from Hinode/SOT–SP 2006/12/13 ~04h UT

f1.eps

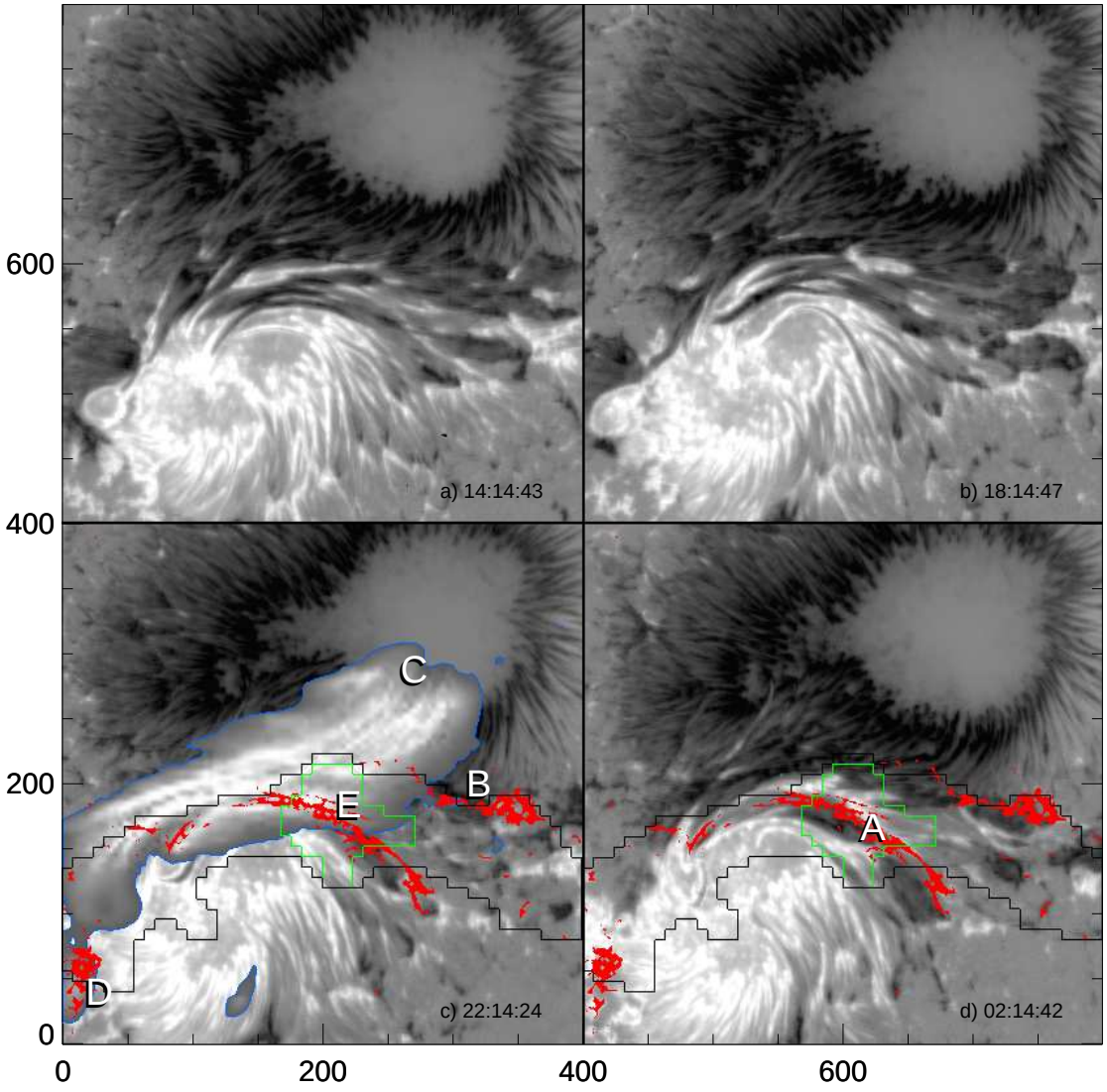
a) 14:14:43
b) 18:14:47
c) 22:14:24
d) 02:14:42
A
B
C
D
E
0
200
400
600
0
200
400
600

f2.ps

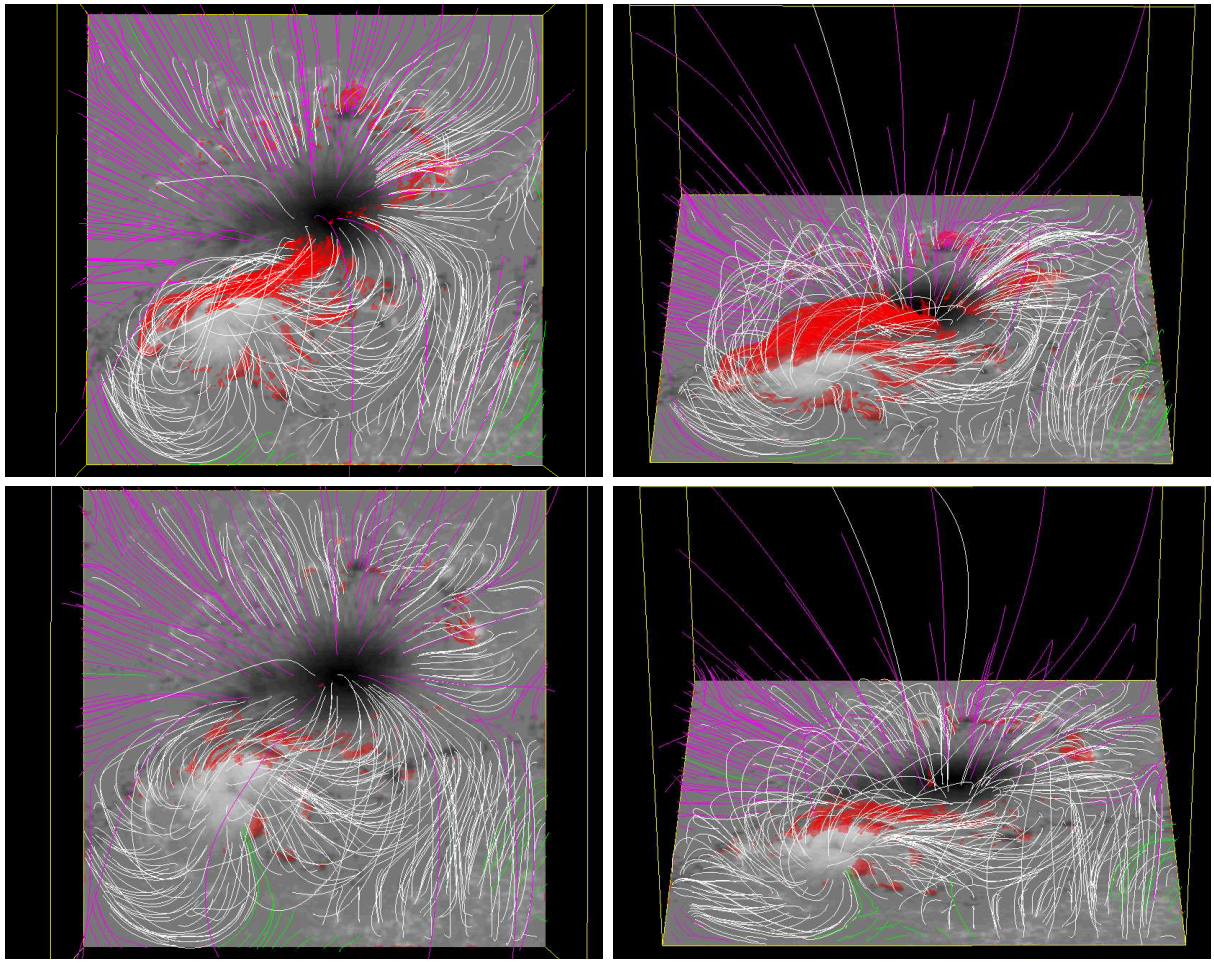

f3[a,b,c,d].eps

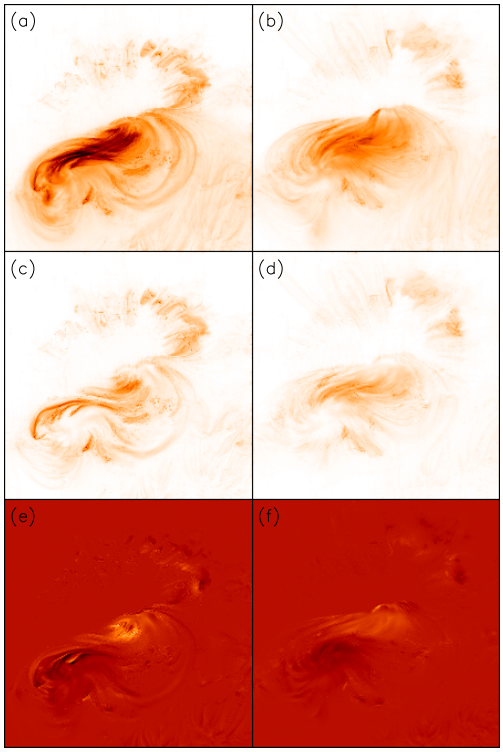

f4.ps